Acta Cryst A FOUNDATIONS ADVANCES
ISSN 2053-2733

Experimentally obtained and computer-simulated X-ray non-coplanar 18-beam pinhole topographs for a silicon crystal

Kouhei Okitsu,[a]* Yasuhiko Imai[b] and Yoshitaka Yoda[b]

[a]Nano-Engineering Research Center, Institute of Engineering Innovation, Graduate School of Engineering, The University of Tokyo, 2-11-16 Yayoi, Bunkyo-ku, Tokyo 113-8656, Japan, and [b]Japan Synchrotron Radiation Research Institute, SPring-8, 1-1-1 Kouto, Mikazuki-cho, Sayo-gun, Hyogo 679-5198, Japan. *Correspondence e-mail: okitsu@soyak.t.u-tokyo.ac.jp

Received 24 September 2018
Accepted 26 February 2019

Edited by P. R. Willmott, Swiss Light Source, Switzerland

This article is dedicated to Professor K. Kohra, who passed away on 29 January 2019.

Keywords: X-ray diffraction; dynamical theory; multiple reflection; *n*-beam reflection; phase problem; protein crystallography.

Non-coplanar 18-beam X-ray pinhole topographs for a silicon crystal were computer simulated by fast Fourier transforming the X-ray rocking amplitudes that were obtained by solving the *n*-beam (n = 18) Ewald–Laue dynamical theory (E-L&FFT method). They were in good agreement with the experimentally obtained images captured using synchrotron X-rays. From this result and further consideration based on it, it has been clarified that the X-ray diffraction intensities when n X-ray waves are simultaneously strong in the crystal can be computed for any n by using the E-L&FFT method.

1. Introduction

The present authors have reported coplanar eight-beam pinhole topographs experimentally obtained and computer simulated by fast Fourier transforming (FFT) the rocking amplitudes calculated based on the *n*-beam Ewald–Laue (E-L) theory. This technique (E-L&FFT simulation) was reported by Kohn & Khikhlukha (2016) and Kohn (2017). In Okitsu *et al.* (2019), it was shown that the E-L&FFT simulation can also be performed for a case where the X-rays do not exit from a single plane (hereafter this paper is denoted as O *et al.* 2019). Furthermore, the feasibility of calculating the X-ray intensities diffracted from a crystal that has plural facets, as shown in Fig. 9 of O *et al.* (2019), was discussed. In addition to this, if the E-L&FFT simulation could be performed even for a case where $n \neq \{3, 4, 5, 6, 8, 12\}$ (non-coplanar case), the intensities of X-ray diffraction spots from a lysozyme (protein) crystal as shown in Fig. 1(*b*) could be calculated. Here a large number (over 200) of reflected X-ray beams are simultaneously strong.

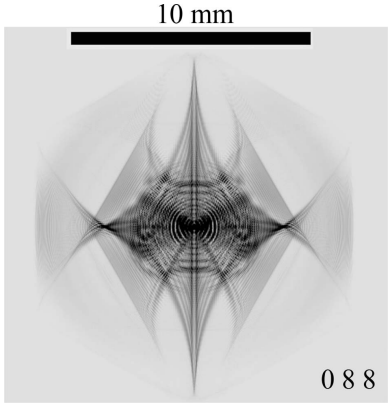

2. Experimental

Fig. 2 shows the experimental arrangement. The horizontally polarized synchrotron X-rays at BL09XU of SPring-8 were monochromated to be 22.0 keV. The phase retarder system was not used in the present experiment. The beam size was limited to 25 × 25 µm. The goniometer system on which a [1$\bar{1}$1]-oriented floating-zone (FZ) silicon crystal was mounted was adjusted such that the 000 forward-diffracted (FD) and 440, 484, 088, $\bar{4}$84 and $\bar{4}$04 transmitted-reflected (TR) X-rays are simultaneously strong; this was achieved by monitoring the 000 FD, 440 and 484 TR X-rays with PIN photodiodes. The thickness of the crystal was 10.0 mm. An imaging plate (IP)

was placed 24 mm behind the crystal such that the surface of the IP was parallel to the exit surface of the crystal.

In addition to the hexagonal six-beam topograph images, a further 12 images surrounding them were found on the IP as shown in Fig. 3(*a*). The exposure time was 300 s.

3. Computer simulation

The length of the wavevector K (= $1/\lambda$, where λ is the wavelength in vacuum) was calculated to be 1.7702394 Å^{-1} for a photon energy of 22.0 keV. The position of the Laue point *La* whose distance from reciprocal-lattice nodes 000, 440, 484, 088, $\bar{4}48$ and $\bar{4}04$ was an identical value K, was calculated on a computer. From Fig. 3(*a*), other reciprocal-lattice nodes were likely to exist in the vicinity of the surface of the Ewald sphere; that is, their distance from *La* was approximately $|na^*| \leq 2K$, *i.e.* $|n| \leq 2a/\lambda$ is the sufficient condition for a reciprocal-lattice node with indices *hkl* to exist on the surface of the Ewald sphere. Here, a is the lattice constant of the silicon crystal, $a^* = 1/a$ and $n \in \{h, k, l\}$. Because $2a/\lambda$ was calculated to be 18.21, the distances of reciprocal-lattice nodes with indices *hkl* from *La* were calculated in the range of $-18 \leq n \leq 18$. Then, in addition to the six reciprocal-lattice nodes, others with $i \in \{6, 7, 8, \ldots, 17\}$ were observed, as summarized in Table 1. Here, i is the ordinal number of the reciprocal-lattice node in the first column of Table 1. Then, all topograph patterns surrounding 000 FD, 440, 484, 088, $\bar{4}48$ and $\bar{4}04$ TR images have been indexed as shown in Fig. 3(*b*). For obtaining this figure, a photon energy of 21.98415 keV was assumed. It was observed that the ith reciprocal-lattice nodes ($i \in \{6, 7, 8, \ldots, 17\}$) were on another circle (drawn as a blue circle in Fig. 4) outside the circle (drawn as a red circle whose centre is Q in Fig. 4) on which the inner six reciprocal-lattice nodes are present. For these 18 FD or TR X-ray beams with indices h_i, k_i, l_i ($i \in \{0, 1, 2, \ldots, 17\}$), the Bragg reflection angle (θ_{B_i}), Θ_i, $\Delta K_i/K$, ϕ_i and χ_{h_i} were calculated and are summarized in Table 1. Θ_i is the angle spanned by $\overrightarrow{LaQ}$ and $\overrightarrow{LaH_i}$ where H_i is the ith-numbered reciprocal-lattice node in Fig. 4. $\Delta K_i/K = (|\overrightarrow{LaH_i}| - K)/K$. ϕ_i is the inclination angle of $\overrightarrow{LaQ} \times \overrightarrow{LaH_i}$ from $\overrightarrow{LaQ} \times \overrightarrow{LaH_0}$.

Fig. 5 is a drawing around the Laue point *La*. Here, let another Laue point La_i' be defined in the vicinity of *La* as shown in Fig. 5 such that $|\overrightarrow{La_i'H_i}| = K$. Because Q is the

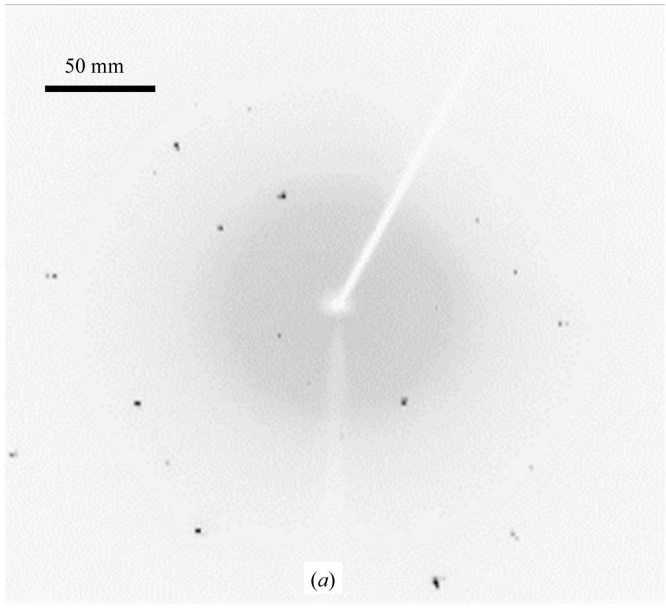

Figure 1
Diffraction spots for (*a*) a sucrose (small molecular weight) crystal and (*b*) a hen egg-white lysozyme (protein) crystal taken on the imaging plate (IP) of a Rigaku Micro7 HFM-AXIS7 diffractometer. The distance between the crystal and the IP was 150 mm. The IP was exposed for 60 s by oscillating the crystal in the range of 0.1° for both (*a*) and (*b*).

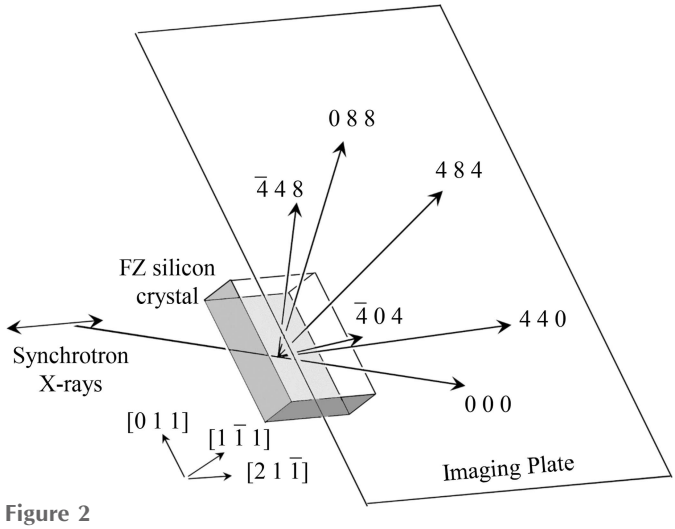

Figure 2
Schematic drawing of the experimental setup. The horizontally polarized synchrotron X-rays were incident on a [1$\bar{1}$1]-oriented floating-zone (FZ) silicon crystal with a thickness of 10.0 mm such that the six beams are simultaneously strong. The angle of the monochromator was adjusted such that the photon energy of the X-rays was 22.0 keV. However, the practical value of the photon energy was considered to be marginally different from this value. An IP was placed 24 mm behind the crystal.

circumcentre of the normal hexagon whose vertices are H_i ($i \in \{0, 1, 2, 3, 4, 5\}$) as shown in Fig. 4, $\overrightarrow{LaLa_i'}$ is evidently $\overrightarrow{0}$ for $i \in \{0, 1, 2, 3, 4, 5\}$ and is an identical vector in the direction of $\overrightarrow{LaQ}/|\overrightarrow{LaQ}|$ ($= \mathbf{n}_z$) for $i \in \{6, 7, \ldots, 17\}$. Here, let ξ_i'' be defined such that $\xi_i''\mathbf{n}_z = \overrightarrow{LaLa_i'}$ as shown in Fig. 5. $k_i - K$ on the left-hand side of equation (4) in O *et al.* 2019 can be described as follows:

$$k_i - K = \mathbf{s}_i \cdot \overrightarrow{P_1'La_i'} \quad (1)$$

$$= \mathbf{s}_i \cdot \left(\overrightarrow{P_1'P_1} + \overrightarrow{P_1La} + \overrightarrow{LaLa_i'}\right). \quad (2)$$

Because $\overrightarrow{P_1'P_1} = \xi\mathbf{n}_z$, $\overrightarrow{P_1La} = K\beta^{(0)}\mathbf{e}_0^{(0)} + K\beta^{(1)}\mathbf{e}_0^{(1)}$ and $\overrightarrow{LaLa_i'} = \xi_i''\mathbf{n}_z$, where $\beta^{(0)}$ and $\beta^{(1)}$ are the two-dimensional angular deviation of P_1 from La as shown in Fig. 5. Therefore, equation (2) can be modified as follows:

$$k_i - K = \mathbf{s}_i \cdot \left(\xi\mathbf{n}_z + K\beta^{(0)}\mathbf{e}_0^{(0)} + K\beta^{(1)}\mathbf{e}_0^{(1)} + \xi_i''\mathbf{n}_z\right) \quad (3)$$

$$= \xi\cos\Theta_i + K\left(S_{i,0}^{(0)}\beta^{(0)} + S_{i,0}^{(1)}\beta^{(1)}\right) + \xi_i''\cos\Theta_i. \quad (4)$$

The polarization factors C and S are defined as

$$\mathbf{e}_j^{(m)} = S_{i,j}^{(m)}\mathbf{s}_i + C_{i,j}^{(0,m)}\mathbf{e}_i^{(0)} + C_{i,j}^{(1,m)}\mathbf{e}_i^{(1)}. \quad (5)$$

In the present 18-beam case, $\mathbf{e}_i^{(0)}$ was defined to be $\mathbf{s}_i \times \mathbf{s}_{\mathrm{mod}(i+3,6)}/|\mathbf{s}_i \times \mathbf{s}_{\mathrm{mod}(i+3,6)}|$ for $i \in \{0, 1, 2, 3, 4, 5\}$ and to be $\mathbf{s}_i \times \mathbf{s}_{[\mathrm{mod}(i,12)+6]}/|\mathbf{s}_i \times \mathbf{s}_{[\mathrm{mod}(i,12)+6]}|$ for $i \in \{6, 7, 8, \ldots, 17\}$. $\mathbf{e}_i^{(1)}$ was defined to be $\mathbf{s}_i \times \mathbf{e}_i^{(0)}$ for $i \in \{0, 1, 2, \ldots, 17\}$.

Laue's fundamental equation of the dynamical theory (von Laue, 1931; Authier, 2005) restricts the amplitude and wavevector of the Bloch wave as follows:

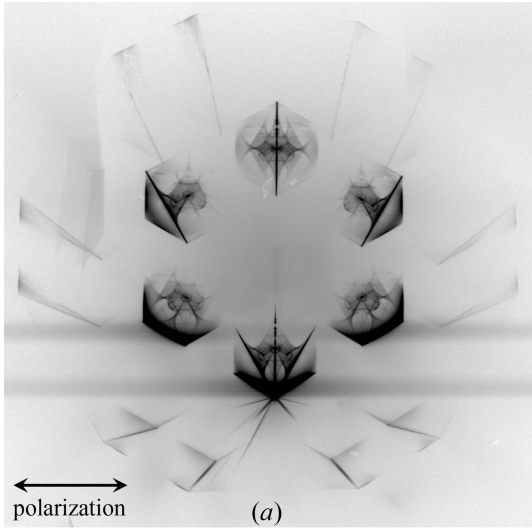

Figure 3
(*a*) Experimentally obtained and (*b*) E-L&FFT simulated 18-beam pinhole topographs. (*b*) was obtained by the E-L&FFT simulation under an assumption of an incidence of X-rays with a photon energy E = 21.98415 keV ($\Delta E = E - E_0 = -0.25$ eV, where E_0 = 21.98440 keV).

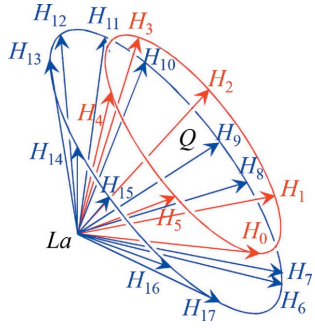

Figure 4
Six reciprocal-lattice nodes are on a red circle in reciprocal space. Outside of this circle, a blue circle was observed on which 12 reciprocal-lattice nodes were present. Q is the centre of the red circle.

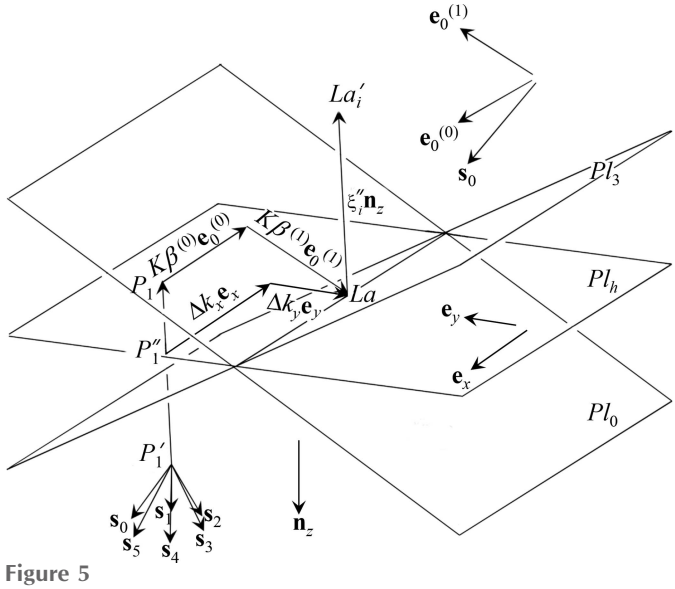

Figure 5
Geometry around the Laue point La. Pl_0 and Pl_3 are planes whose distance from H_0 and H_3 is K. Pl_h is a plane normal to $\mathbf{n}_z$ (downward surface normal). The Laue point La and point P_1'' exist on Pl_h. Pl_i ($i \in \{1, 2, 4, 5, \ldots, 17\}$) were not drawn for simplicity. La_i' is a point whose distance from H_i ($i \in \{6, 7, \ldots, 17\}$) is K. P_1' is the initial point of the wavevector of the Bloch wave. $P_{1,k}'$ that appears in equation (14) in O *et al.* (2019) is the kth-numbered P_1', *i.e.* the initial point of the wavevector of the kth-numbered Bloch wave where $k \in \{1, 2, 3, \ldots, 2n\}$.

Table 1
The position of the point *La* whose distance from the *i*th-numbered reciprocal-lattice nodes H_i ($i \in \{0, 1, 2, 3, 4, 5\}$) is an identical length K, calculated for a photon energy of 22.0 keV.

The Miller indices were 000, 440, 484, 088, $\bar{4}40$ and $\bar{4}04$. Θ_i (°) ($i \in \{0, 1, 2, \ldots, 17\}$) is the angle spanned by the directions of $\mathbf{n}_z$ and $\overrightarrow{LaH_i}$. $\mathbf{n}_z$ is a unit vector in the direction of $[1\bar{1}1]$ (downward surface normal). When $K_i = |\overrightarrow{LaH_i}|$, $\Delta K_i/K = (K_i - K)/K$. ϕ_i is the inclination angle of $\mathbf{n}_z \times \overrightarrow{LaH_i}$ from $\mathbf{n}_z \times \overrightarrow{LaH_0}$. $\chi_{h_i}^{(\mathrm{r})}$ and $\chi_{h_i}^{(\mathrm{i})}$ are, respectively, the real and imaginary parts of the $\mathbf{h}_i$th-order Fourier coefficient of the electric susceptibility as calculated using *XOP 2.3* (Sanchez del Rio & Dejus, 1998) for a photon energy of 22.0 keV. Identical values of $\chi_{h_i}^{(\mathrm{r})}$ and $\chi_{h_i}^{(\mathrm{i})}$ were used for all the simulations shown in Figs. 3, 6 and 7 because the energy differences from 22.0 keV are negligible.

Ordinal number i	h_i	k_i	l_i	θ_{B_i} (°)	Θ_i (°)	$\Delta K_i/K \times 10^4$	ϕ_i (°)	$\chi_{h_i}^{(\mathrm{r})} \times 10^6$	$\chi_{h_i}^{(\mathrm{i})} \times 10^8$
0	0	0	0	0.0000	35.9750	0.0000	0.0000	−2.004400	−0.625153
1	4	4	0	17.0806	35.9750	0.0000	60.0000	−0.773093	−0.550274
2	4	8	4	30.5793	35.9750	0.0000	120.0000	−0.296936	−1.136870
3	0	8	8	35.9750	35.9750	0.0000	180.0000	−0.214413	−0.375281
4	$\bar{4}$	4	8	30.5793	35.9750	0.0000	240.0000	−0.296936	−0.426348
5	$\bar{4}$	0	4	17.0806	35.9750	0.0000	300.0000	−0.773093	−0.550274
6	1	1	$\bar{3}$	9.9161	50.9503	−1.5751	19.1066	−0.784785	−0.423082
7	3	3	$\bar{3}$	15.6521	50.9503	−1.5751	40.8934	+0.586813	+0.396937
8	5	7	$\bar{1}$	26.7218	50.9503	−1.5751	79.1066	+0.285189	+0.327801
9	5	9	1	32.4855	50.9503	−1.5751	100.8933	−0.183684	−0.288538
10	3	11	5	40.2726	50.9503	−1.5751	139.1066	+0.128538	+0.238282
11	1	11	7	42.7632	50.9503	−1.5751	160.8934	+0.116815	+0.223557
12	$\bar{3}$	9	9	42.7632	50.9503	−1.5751	199.1066	−0.116815	−0.223557
13	$\bar{5}$	7	9	40.2726	50.9503	−1.5751	220.8934	+0.128538	+0.238282
14	$\bar{7}$	3	7	32.4855	50.9503	−1.5751	259.1066	+0.183684	+0.288538
15	$\bar{7}$	1	5	26.7218	50.9503	−1.5751	280.8934	−0.285189	−0.327801
16	$\bar{5}$	$\bar{1}$	1	15.6521	50.9503	−1.5751	319.1066	+0.586813	+0.396937
17	$\bar{3}$	$\bar{1}$	$\bar{1}$	9.9161	50.9503	−1.5751	340.8934	−0.784785	−0.423082

Table 2
Values of ξ_i'' for $\Delta E (= E - E_0)$ are −0.75, −0.50, −0.25, 0.00, +0.25, +0.50 and +0.75 eV, where E_0 = 21.98440 keV.

Fig. No. of the simulation	Photon energy E (keV)	$E - E_0$ ΔE (eV)	ξ_i'' (m^{-1})
Fig. 6(*a*)	21.98365	−0.75	+2.11782 × 10^5
Fig. 6(*b*)	21.98390	−0.50	+1.40582 × 10^5
Fig. 3(*b*)	21.98415	−0.25	+0.69386 × 10^5
Fig. 6(*c*)	21.98440	0.00	0.01805 × 10^5
Fig. 6(*d*)	21.98465	+0.25	−0.72993 × 10^5
Fig. 6(*e*)	21.98490	+0.50	−1.44176 × 10^5
Fig. 6(*e*)	21.98515	+0.75	−2.15356 × 10^5

$$\frac{k_i^2 - K^2}{k_i^2}\boldsymbol{D}_i = \sum_{j=0}^{n-1} \chi_{h_i - h_j}\left[\boldsymbol{D}_j\right]_{\perp \mathbf{k}_i}. \tag{6}$$

Here $K = 1/\lambda$, where λ is the wavelength of the X-rays in vacuum, and $[\boldsymbol{D}_j]_{\perp \mathbf{k}_i}$ is the component vector of $\boldsymbol{D}_j$ perpendicular to $\mathbf{k}_i$. By applying the approximation $k_i + K \simeq 2K$, equation (6) becomes

$$(k_i - K)\boldsymbol{D}_i = \frac{K}{2}\sum_{j=0}^{n-1} \chi_{h_i - h_j}\left[\boldsymbol{D}_j\right]_{\perp \mathbf{k}_i}. \tag{7}$$

Substituting equation (4) into equation (7), the following equation can be obtained:

$$\xi\mathcal{D}_i^{(l)} = -\left[K\left(S_{i,0}^{(0)}\beta^{(0)} + S_{i,0}^{(1)}\beta^{(1)}\right)/\cos\Theta_i + \xi_i''\right]\mathcal{D}_i^{(l)} + \frac{K}{2\cos\Theta_i}\sum_{j=0}^{n-1}\chi_{h_i - h_j}\sum_{m=0}^{1} C_{i,j}^{(l,m)}\mathcal{D}_j^{(m)}. \tag{8}$$

Equation (8) is represented by using a vector and a matrix as follows:

$$\xi\boldsymbol{D} = \boldsymbol{A}'\boldsymbol{D}. \tag{9}$$

Here $\boldsymbol{D}$ is a $2n$-order column vector and $\boldsymbol{A}'$ is a $2n \times 2n$ matrix whose element in the pth row ($p = 2i + l + 1$) and qth column ($q = 2j + m + 1$) $\mathcal{A}'_{p,q}$ is given by

$$\mathcal{A}'_{p,q} = K\chi_{h_i - h_j}C_{i,j}^{(l,m)}/(2\cos\Theta_i) - \delta_{p,q}\left[K\left(S_{i,0}^{(0)}\beta^{(0)} + S_{i,0}^{(1)}\beta^{(1)}\right)/\cos\Theta_i + \xi_i''\right]. \tag{10}$$

Here, $\delta_{p,q}$ is the Kronecker delta. Moreover, for the present 18-beam case, the procedure described by equations (10)–(16) in O *et al.* 2019 can be used to solve the eigenvalue problem of equations (9) and (10). The values of Θ_i, $\chi_{h_i - h_j}$ and ξ_i'' listed in Tables 1 and 2 were used.

Furthermore, for the FFT to compute the E-L&FFT topographs, the description using equations (17)–(20) in O *et al.* 2019 can also be applied to the present 18-beam case. The FFT in equation (20) in O *et al.* 2019 was carried out with L = 50 mm and N = 4096.

It required 1080 s (890 s for solving the eigenvalue problem, 20 s for FFT and 170 s for writing the topographs to the hard disk) to obtain the 18 topograph images shown in Fig. 3(*b*) using one node (Intel Xeon E5-2680v3) of the supercomputer system 'Sekirei' of the Institute of Solid State Physics of the University of Tokyo. The calculation to solve the eigenvalue problem for a 36 × 36 matrix was several times as time-consuming as the coplanar eight-beam case solving the eigenvalue problem described with two 16 × 16 matrices described in O *et al.* 2019.

4. Results

Fig. 6(*c*) shows the E-L&FFT simulated result with a photon energy of 21.98440 keV. In this figure, X-ray diffraction intensities due to the outer 12 reciprocal-lattice nodes on the blue circle in Fig. 4 are as strong as the inner six diffraction patterns that are substantially different from the experimentally obtained topograph in Fig. 3(*a*). However, the outer 12 topograph patterns are almost unobservable when the energy deviation from E_0 (= 21.98440 keV) is over 0.50 eV. Thus the present authors conclude that the photon energy of the synchrotron X-rays used in the present experiment was ∼21.98415 keV with which Fig. 3(*a*) was obtained.

Fig. 7 shows enlargements of 088 TR and 000 FD images from Figs. 3(*a*) and 3(*b*). There is remarkable consistency between the experimentally obtained and the E-L&FFT simulated images.

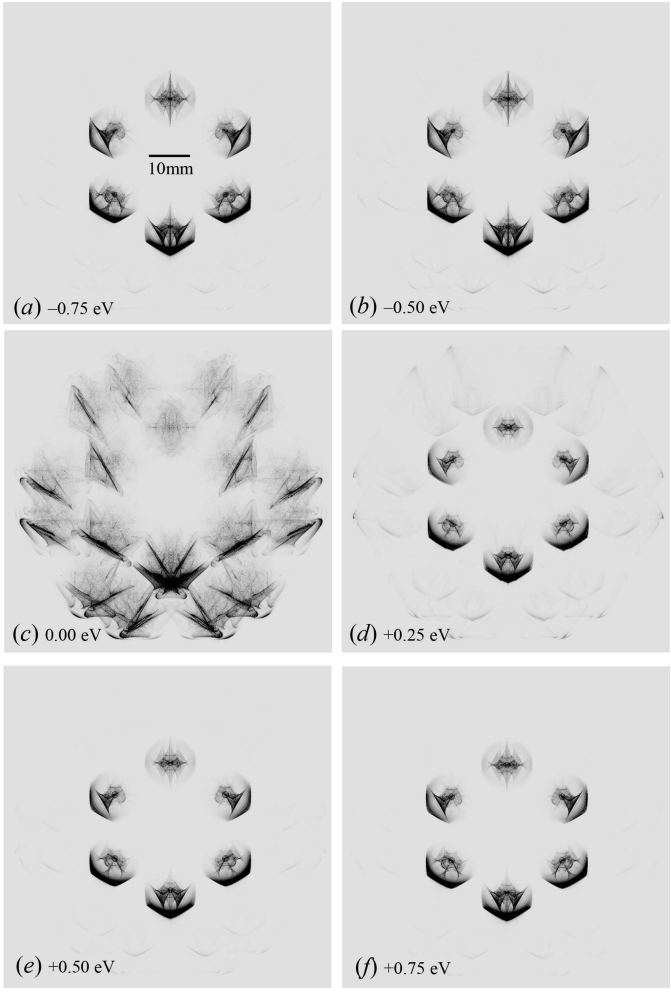

Figure 6
When the photon energy is 21.9843937 keV, the inner six and outer 12 reciprocal-lattice nodes (see Fig. 4) can be present simultaneously on an identical surface of the Ewald sphere. The deviations of photon energies from E_0 (= 21.98440 keV) were assumed to be −0.75, −0.50, 0.00, +0.25, +0.50 and +0.75 eV for (*a*), (*b*), (*c*), (*d*), (*e*) and (*f*), respectively.

5. Discussion

Fig. 8 shows an image of 088 TR X-rays obtained by the E-L&FFT simulation omitting the presence of the outer 12 reciprocal-lattice nodes. The assumed photon energy was identical to that in Fig. 7 [*S*(*a*)] (21.984150 keV). The vertical centre line in Fig. 8 was divided into two lines, whereas only one vertical line was observed in Fig. 7 [*S*(*a*)]. Further, an evident difference in the central part was observed between Fig. 7 [*S*(*a*)] and Fig. 8. It has been clarified that the presence of the outer 12 reciprocal-lattice nodes affected the features of the inner six diffraction patterns.

Incidentally, referring to Fig. 5, let another Laue point La_0'' be defined at a position on Pl_0 such that it is not far from La and $\overrightarrow{P_1La_0''} = K\beta^{(0)\prime}\mathbf{e}_0^{(0)} + K\beta^{(1)\prime}\mathbf{e}_0^{(1)}$. Further, let La_i'' be defined such that $\overrightarrow{La_0''La_i''} = \xi_i'''\mathbf{n}_z$ on Pl_i whose distance from H_i is K ($i \in \{0, 1, 2, \ldots, n-1\}$). By replacing $\beta^{(0)}$, $\beta^{(1)}$ and ξ_i'' in equations (9) and (10) with $\beta^{(0)\prime}$, $\beta^{(1)\prime}$ and ξ_i''', respectively, the following equation is obtained:

$$\xi \boldsymbol{D}' = \boldsymbol{A}''\boldsymbol{D}'. \tag{11}$$

Here, $\boldsymbol{D}'$ is a $2n$-order column vector and $\boldsymbol{A}''$ is a $2n \times 2n$ matrix whose element in the pth row ($p = 2i + l + 1$) and qth column ($q = 2j + m + 1$) $\mathcal{A}_{p,q}''$ is given by

$$\mathcal{A}_{p,q}'' = K\chi_{h_i-h_j}C_{i,j}^{(l,m)}/(2\cos\Theta_i) - \delta_{p,q}\left[K\left(S_{i,0}^{(0)}\beta^{(0)\prime} + S_{i,0}^{(1)}\beta^{(1)\prime}\right)/\cos\Theta_i + \xi_i'''\right]. \tag{12}$$

This way of defining La_i'', $\beta^{(0)\prime}$, $\beta^{(1)\prime}$, ξ_i''' and $\boldsymbol{A}''$ and equations (11) and (12) are more general than equations (9) and (10).

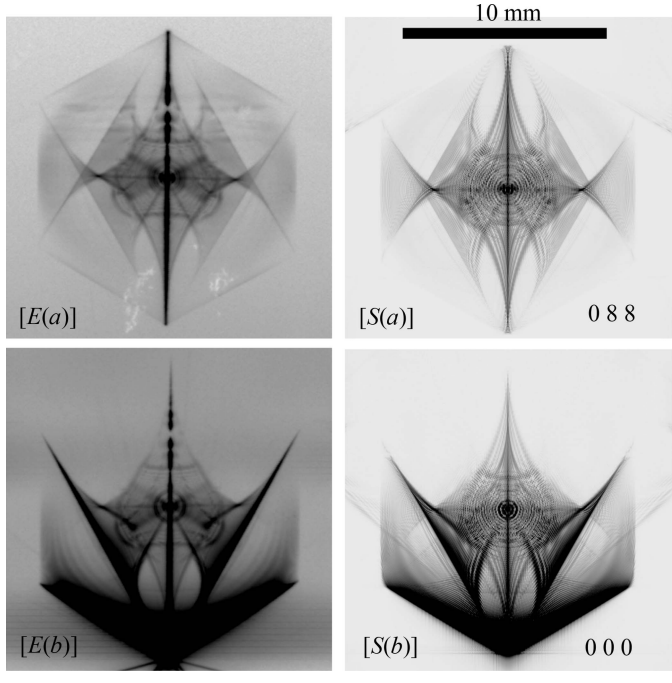

Figure 7
[*E*(*a*)] and [*E*(*b*)] are enlargements of 088 TR and 000 FD X-ray patterns of Fig. 3(*a*) obtained experimentally. [*S*(*a*)] and [*S*(*b*)] are enlargements of 088 TR and 000 FD X-ray patterns of Fig. 3(*b*) obtained by the E-L&FFT simulation.

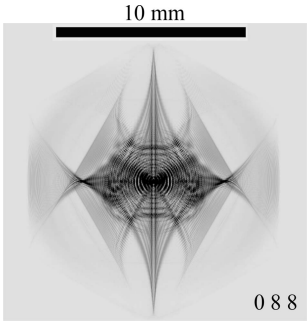

Figure 8
E-L&FFT simulated 088 TR topograph images with a photon energy of 21.98415 keV under an assumption of the six-beam case; here, the 000 FD, 440, 484, 088, $\bar{4}48$ and $\bar{4}04$ TR X-rays are strong by neglecting the outer 12 beams. An evident discrepancy is observed between this figure and Fig. 7 [$S(a)$].

Even when La cannot be defined as shown in Fig. 5, the eigenvalue problem represented by (11) can be solved. Then, the intensity distribution of reflected X-rays can be calculated with the E-L&FFT method when a pinhole X-ray beam is incident on an arbitrary position of the surface of the crystal. This is also the case for a crystal as shown in Fig. 9 of O *et al.* 2019 owing to the description given therein. The total intensities of X-rays reflected from the crystal completely bathed in the incident X-rays can be calculated by incoherently superposing the pinhole topograph intensities with the incident position two-dimensionally scanned over the incident side of the crystal.

6. Summary

In the present non-coplanar 18-beam case, the 18 reciprocal-lattice nodes are on two circles, drawn in red and blue in Fig. 4. The most important aspect of the present work is that a non-coplanar n-beam case for $n \neq \{3, 4, 5, 6, 8, 12\}$ was computer simulated using the E-L&FFT method and was reasonably consistent with the experimentally obtained result. The constraint that $n \in \{3, 4, 5, 6, 8, 12\}$ has been originally placed such that n reciprocal-lattice nodes are on a circle in the reciprocal space. In the case of protein crystals as shown in Fig. 1(b), the situation where a large number of reciprocal-lattice nodes are simultaneously present in the vicinity of the surface of the Ewald sphere cannot be circumvented.

However, the constraint on n has been removed completely from the n-beam E-L&FFT method to calculate the X-ray diffraction intensities. N is the number of reciprocal-lattice nodes present in the vicinity of the surface of the Ewald sphere whose presence should be considered. Another difficulty caused by the complex shape of the crystal has also been overcome with the description in O *et al.* 2019. Thus, the present authors could calculate the intensities of X-ray diffraction spots as shown in Fig. 1(b) under the assumption that the crystal is perfect.

Acknowledgements

The SGI ICE XA supercomputer system 'Sekirei', which consists of Intel Xeon E5-2680v3 processors, of the Institute for Solid State Physics of the University of Tokyo was used for the computer simulation. The experiment was performed at BL09XU of SPring-8 under the approval of the Japan Synchrotron Radiation Research Institute (JASRI) (Proposal No. 2009B1384). The authors are indebted to Dr T. Oguchi and Dr G. Ishiwata for their technical support in the present experiments and also to Professor Emeritus S. Kikuta for his encouragement and effective discussions with respect to the present work.

Funding information

The theoretical part and computer simulation of the present work were supported by the Nanotechnology Platform Project (No. 12024046) of the Ministry of Education, Culture, Sports, Science and Technology (MEXT), Japan.

References

Authier, A. (2005). *Dynamical Theory of X-ray Diffraction*. Reprinted with revisions 2004, 2005. Oxford University Press.
Kohn, V. G. (2017). *Acta Cryst.* A**73**, 30–38.
Kohn, V. G. & Khikhlukha, D. R. (2016). *Acta Cryst.* A**72**, 349–356.
Laue, M. von (1931). *Ergeb. Exakten Naturwiss*, **10**, 133–158.
Okitsu, K., Imai, Y., Yoda, Y. & Ueji, Y. (2019). *Acta Cryst.* A**75**, 474–482.
Sanchez del Rio, M. & Dejus, R. J. (1998). *Proc. SPIE*, **3448**, 340–345.